Estimate of entropy production rate can spatiotemporally resolve the active nature of cell flickering

Sreekanth K. Manikandan,[1,2,*] Tanmoy Ghosh,[3] Tithi Mandal,[3] Arikta Biswas,[3,†]
Bidisha Sinha,[3,‡] and Dhrubaditya Mitra[2,§]

[1]*Department of Chemistry, Stanford University, Stanford, California 94305, USA*
[2]*NORDITA, KTH Royal Institute of Technology and Stockholm University, Roslagstullsbacken 23, 10691 Stockholm, Sweden*
[3]*Department of Biological Sciences, Indian Institute of Science Education and Research Kolkata, Mohanpur, Nadia–741246, India*

(Received 29 August 2022; accepted 13 May 2024; published 21 June 2024)

We use the short-time inference scheme [Manikandan *et al.*, Phys. Rev. Lett. **124**, 120603 (2020)], obtained within the framework of stochastic thermodynamics, to infer a lower bound to entropy production rate from flickering data generated by interference reflection microscopy of HeLa cells. We can clearly distinguish active cell membranes from their adenosine-triphosphate-depleted selves and even spatiotemporally resolve activity down to the scale of about 1 μm. Our estimate of activity is *model independent*.

DOI: 10.1103/PhysRevResearch.6.023310

I. INTRODUCTION

At the dawn of biophysical research [1], it was already realized that the fundamental property of living cells is that they are not in thermal equilibrium even when they are statistically stationary—they consume energy and generate entropy; see, e.g., Ref. [2] for a recent review. Nevertheless, tools of equilibrium physics are frequently used to interpret results of experiments on living cells; for example, equilibrium models are used to infer bending rigidity from flickering data—vibrating fluctuations of a cell membrane; see, e.g., Ref. [3] for this and several other examples. Although the possible influence of active transport on flickering was first pointed out at least 70 years ago [4], investigation into the essential nonequilibrium feature of flickering, by comparing flickering data from a healthy cell with its adenosine triphosphate (ATP)-depleted self, has peaked in the last two decades [5–7], see also Ref. [8] and references therein. For red blood cells (RBCs), the first unequivocal demonstration of their nonequilibrium nature was shown via the violation of the fluctuation-dissipation theorem [9]. However, no attempt has been made so far to spatiotemporally resolve, from flickering data, the fundamental physical quantity that characterizes nonequilibrium, viz., the rate of entropy production σ.

On the one hand, recent spectacular progress in visualizing and tracking biological processes [10–14] with unprecedented accuracy and control raises hopes that measuring entropy production rate for cellular processes is indeed possible. On the other hand, there are several difficulties: (a) They are small in magnitude, of the order of few $k_B\,s$ per second, and lie below the threshold of detection for the existing calorimetric techniques [15]. (b) Thermal fluctuations cannot be ignored, hence any measurement results in noisy readings [16]. (c) Typically, we have access to only a few degrees of freedom, e.g., flickering gives us access to the fluctuations of the cell membrane down to a certain length and time scale, while fluctuations at smaller length and time scales and the motion of the cytoskeleton that drives flickering are not accessible. (d) In far-from-equilibrium regimes, there are very few general principles.

The theoretical understanding of the far-from-equilibrium behavior of microscopic systems has undergone a revolution over the last two decades [17,18], giving rise to the subfield of statistical physics called *stochastic thermodynamics*, which can in principle extract entropy production rate from long-enough stochastic trajectories of *all the degrees of freedom* of the system [18,19]. With limited data—limited in both time and number of accessible degrees of freedom—the best we can do is to set bounds [20–34].

In this paper, we use a recent addition to this list of techniques, *the short-time inference scheme* [29,35,36], together with flickering data of HeLa cells to estimate spatiotemporally resolved entropy production rate. As the entropy production rate is the fundamental characteristic of the active nature of the fluctuations, in the rest of this paper we shall use the word activity and entropy production rate interchangeably. The short-time inference scheme is built on the thermodynamic uncertainty relation [22], which states that a lower bound to the entropy production rate can be obtained via fluctuations of any arbitrary current J in phase space, as

$$\sigma \geqslant 2k_B \frac{\langle J\rangle^2}{t\ \mathrm{Var}(J)}, \tag{1}$$

where $\langle\cdot\rangle$ and $\mathrm{Var}(\cdot)$ denote mean and variance of a random variable calculated from a statistically stationary time series

*Contact author: sreekm@stanford.edu
†Present address: Mechanobiology Institute National University of Singapore 5A Engineering Drive, Singapore 117411.
‡Contact author: bidisha.sinha@iiserkol.ac.in
§Contact author: dhrubaditya.mitra@su.se

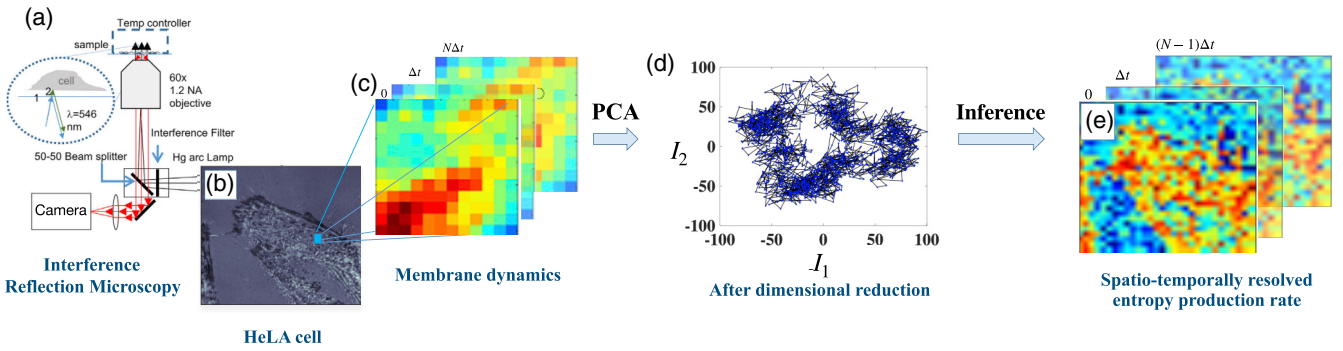

FIG. 1. We use interference reflection microscopy (a) to obtain flickering data from the basal membrane of HeLa cells (b) with a patch marked by a sky blue square. Zoomed-in picture of the patch in (c) typically contains $M^2 = 400$ pixels. The 400 time series are dimensionally reduced to a few by principal component analysis (PCA). (d) The stochastic trajectory of the first two principal components for a typical case. We obtain the entropy production rate σ by numerical optimization of this reduced problem. Using the first six principal components instead of the first two has a negligible effect on our results. Color map of σ in (e) clearly shows the active cells compared to its background. The sketch in (a) is adapted from Ref. [37].

of phase space trajectories over a time interval t and k_B is the Boltzmann constant. References [29,35,36] extended this result to show that for a large class of nonequilibrium systems with an overdamped Langevin dynamics, the inequality, Eq. (1), saturates in the short time limit, i.e.,

$$\sigma = 2k_B \lim_{\Delta t \to 0} \max_{J} \left[\frac{\langle J_{\Delta t} \rangle^2}{\Delta t \ \mathrm{Var}(J_{\Delta t})} \right]. \tag{2}$$

Here, $J_{\Delta t}$ is calculated over time Δt and the mean and the variance is calculated over an ensemble of such time intervals.

This scheme has certain key advantages over its competitors: one, it is model independent—the precise knowledge of the underlying overdamped Langevin equation is not required; two, it is not limited to stationary time series. This scheme has been successfully used to estimate the entropy production rate from a moderate number of realizations of stochastic trajectories of time-dependent systems [31]. The scheme was also tested experimentally using the stationary trajectories of a colloidal particle in an stochastically shaken optical trap [38]. Here, we apply Eq. (2) to analyze flickering data from living cell membranes.

II. METHODS

In Fig. 1 we pictorially summarize our method. We first obtain a movie of flickering data for the basal membrane, a part of the membrane attached to the substrate, of adherent HeLa cells using interference reflection microscopy (IRM). HeLa cells (CCL-2, ATCC) were grown in Dulbecco's modified essential medium (DMEM, Gibco, Life Technologies, USA) supplemented with 10% fetal bovine serum (FBS, Gibco) and 1% Antibiotic-Antimycotic (Gibco) at 37°C under 5% CO_2. Experiments were always performed after 16–18 h of cell seeding. IRM imaging [37,39] was conducted using a motorized inverted microscope (Nikon, Japan) equipped with adjustable field and aperture diaphragms, a 60× water immersion objective (NA 1.22), 1.5× external magnification, an on-stage 37°C incubator (Tokai Hit, Japan), an s-CMOS camera (ORCA Flash 4.0, Hamamatsu, Japan), a 100-W mercury arc lamp, an interference filter (546 ± 12 nm), and a 50-50 beam splitter [37]. Pixel intensities were converted to relative heights (distance of the membrane from the coverslip) using a MATLAB (MathWorks, USA) code after obtaining the intensity-to-height conversion factor determined by a beads-based calibration method as reported previously [37]. Every experiment was preceded by an independent calibration.

A typical image of a cell is shown in Fig. 1(b). In addition to the cell, the background is also visible. For the analysis, we divide this cell into several square patches of equal size (∼2 μm^2). One such patch is shown as a blue square in Fig. 1(b). Each patch is made of $M \times M$ pixels. Thus, the time evolution of each patch is completely described by M^2 stochastic variables $I = (I_1, I_2, \ldots, I_{M^2})$—the light intensity at each of the pixels. We record movies with a time step $\Delta t = 50$ ms between two consecutive snapshots. A typical movie consists of $N_f = 2048$ snapshots—see Fig. 1(c). In order to apply the inference scheme in (2), in principle, we can calculate currents from two consecutive snapshots and average over the number of snapshots to calculate the quantity inside the square brackets in (2). In that case, we have to perform numerical optimization over M^2 space, which is a formidable problem. Following Ref. [28], we use principal component analysis (PCA) to reduce the dimension of the problem in the following manner. Construct the covariance matrix $\boldsymbol{C}$, with elements $C_{ij} \equiv \langle I_i I_j \rangle - \langle I_i \rangle \langle I_j \rangle$. The average is taken over the number of frames N_f. This is averaging over a time interval, in which the time series is assumed to be stationary. The method applies equally well for ensemble averaging [31]. The projections of the data along the eigenvectors of this covariance matrix, in decreasing magnitude of eigenvalue, are the principal components. Figure 1(d) shows a typical example of the dynamics in the first two components, $\mathcal{I}_1(t)$ and $\mathcal{I}_2(t)$. In general, the state of the system can be projected to any $N \leqslant M^2$-dimensional vector $\boldsymbol{\mathcal{I}} = (\mathcal{I}_1, \ldots \mathcal{I}_\alpha, \ldots \mathcal{I}_N)$. Next, we define a scalar current:

$$J_{\Delta t}(t_i) \equiv \boldsymbol{d}\left(\frac{\boldsymbol{\mathcal{I}}(t_i + \Delta t) + \boldsymbol{\mathcal{I}}(t_i)}{2} \right) \cdot [\boldsymbol{\mathcal{I}}(t_i + \Delta t) - \boldsymbol{\mathcal{I}}(t_i)], \tag{3}$$

where $\boldsymbol{d}(\mathcal{I})$ is *any* arbitrary N-dimensional function. Then, we need to find the optimal function $\boldsymbol{d}^*(\mathcal{I})$ which maximize the bound in (2). We use two different algorithms: (A) We

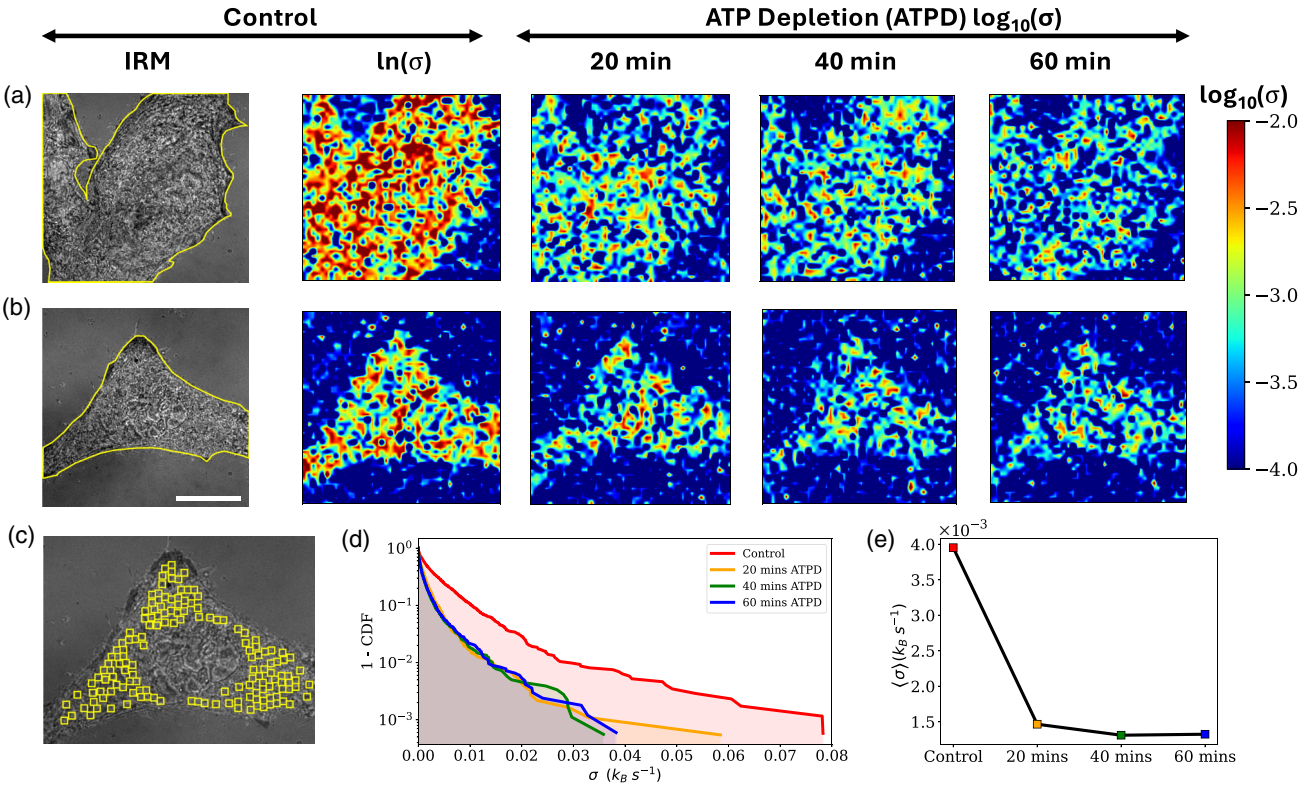

FIG. 2. Activity of cell membrane. (a) and (b) From left to right: Typical IRM image of two live HeLa cells; the boundary of the cells is marked in yellow. Color map of $\ln(\sigma)$ before the cells are treated with ATP-depleting agents. Color map of $\log_{10}(\sigma)$ after incubating the cells in ATP-depleting agents for 20, 40, and 60 min. For clarity, the color map is limited to a fixed range. (c) Representative IRM image of a cell with FBRs (size: 20×20 pixels or $2\,\mu m^2$) marked in yellow. (d) Plot of (1 - CDF) of σ, for the FBR patches, for control and three different durations of ATP depletion. (e) Average of σ over FBR patches under ATP depletion.

use a linear function $d_\alpha(\boldsymbol{\mathcal{I}}) = c_{\alpha\beta}\mathcal{I}_\beta$, where the matrix $c_{\alpha\beta}$ is a matrix of constant coefficients, and perform the optimization by the particle-swarm algorithm. (B) We use a nonlinear function for $\boldsymbol{d}(\mathcal{I})$ represented by a feed–forward neural network $\boldsymbol{d}(\mathcal{I}|\boldsymbol{\theta})$, where θ are the parameters of the network. For a fixed choice of the parameters, the mean and the variance of the current are computed by averaging over the index i. The analysis can then be extended to cells under different physiological conditions and at different times, to obtain a spatiotemporally resolved entropy production map as in Fig. 1(e). Both the algorithms give similar results, with (A) yielding a slightly lower estimate than (B). See Appendix A for details.

III. RESULTS

In Fig. 2(a), we show how our method performs on the experimental data as the cells are ATP-depleted by incubating them in glucose-free ATP-depleting medium. We do this by adding 10 mM sodium azide and 10 mM 2-deoxy D-glucose to the cells [40] in M1 Imaging medium (150 mM NaCl; Sigma-Aldrich), 1 mM MgCl2 (Merck, Kenilworth, NJ), and 20 mM HEPES (Sigma-Aldrich), and incubating them for 60 min for ATP depletion. In recent work by some of the authors, it was found that ATP-driven activities increase temporal fluctuations and flatten out spatial undulations—see Fig. 3 in Ref. [37] and discussions therein for the detailed analysis and discussion on the effect of ATP depletion on membrane fluctuations.

In the leftmost row of Fig. 2 we show the image of the cell—the cell boundaries are marked in yellow. The next column shows a pseudocolor plot of $\log_{10}(\sigma)$ of the live cell, marked by *control*. The next three columns show how the entropy production rate changes after 20 min, 40 min, and 1 h of incubation. In each of these cases, we use a movie of $N_f = 2048$ snapshots where consecutive snapshots are separated by $\Delta t = 50\,\text{ms}$. Since the total duration of the movie is quite short compared to the time scales over which ATP depletion operates, each of these movies are considered statistically stationary. We have performed these experiments for a total of 31 HeLa cells, with two independent repeats. Images of two typical cells are shown in Figs. 2(a) and 2(b). The images of several other representative cases are in the Supplemental Material [41]. Our results clearly demonstrate that the entropy production rate computed using (2) spatiotemporally resolves the active nature of cell membrane fluctuations. Notably, we see many patches of high entropy production in the active cell membrane, which is well contrasted with the background, and patches of low entropy production in the ATP–depleted membrane, less contrasted with the background. We also see an overall decay of σ in time.

To calculate reliable statistical properties of the entropy production rate—for the control and the ATP-depleted ones—we limit ourselves to patches that are inside the cell and away

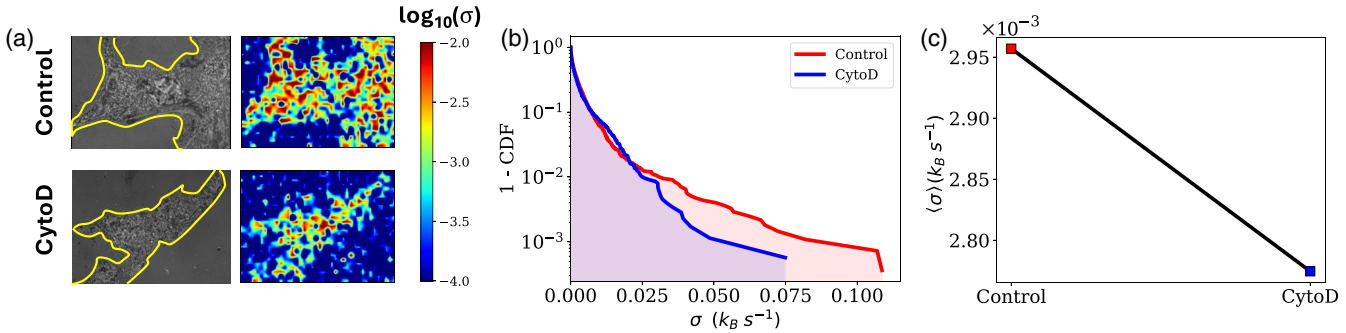

FIG. 3. How Cyto-D affects activity. (a) IRM image and color map of $\log_{10}(\sigma)$ of a HeLa cell from the control set and Cyto-D treated cells. Note that unlike Fig. 2, these two are not the same cell. The boundaries of the cells are marked in yellow. (b) The average as well as the distribution (inset) of σ. Data is representative of three independent experiments on 17 control cells and Cyto-D treated ones. The images of several other representative cases are in the Supplemental Material [41].

from the nucleus; an example is shown in Fig. 2(c). The relative heights of these patches lie within the range ∼0–100 nm—termed as first-branch regions (FBRs). Henceforth we call these patches FBR patches. We use rank-order methods to calculate the cumulative distribution function (CDF) of σ from all the FBR patches of all the cells, see Fig. 2(d). The rank-order method does not suffer from the binning errors that plague histogram-based methods to calculate the probability distribution function. We calculate the probability density function (PDF) of σ by calculating the derivatives of the CDF. The complement of the CDF, defined as 1 - CDF, has an exponential tail to the right. This implies that the PDF of σ also has an exponential tail. In Fig. 2(e) we show how the mean value of the σ decreases under ATP depletion. A straightforward computation of the average σ over all FBR patches for the control cell yields a value of approximately $4 \times 10^{-3}\, k_B\, s^{-1}$ across a patch area of $2\,\mu m^2$. The exponential tail of the PDF implies that σ shows large fluctuations. In particular, the average of the top 10% of patches is nearly five times higher than the mean, and the average of the top 50% of patches is nearly double—see Appendix A 3.

Which processes on the membrane are the major contributors to the measured activity? Of the many ATP-dependent processes that may actively impact membrane fluctuations, forces originating at the underlying actomyosin cortex are important [37,42]. The effect of actin polymerizing forces [43] as well as forces by myosin motor protein contracting the actin network are expected to be diminished if the cortex is weakened or removed. It has been shown [44] that the drug Cytochalasin D (Cyto D) suppresses actin polymerization and weakens the cortical network. This is achieved by treating the cells with 5-μM cytochalasin D (Cyto D, Sigma Aldrich) for 1 h in serum-free media [37]. Its effect on membrane fluctuations was further found to be highly spatially inhomogeneous—see Fig. 4 in Ref. [37] and discussions therein for the detailed analysis and discussion on the effect of Cyto D treatment on membrane fluctuations. The network is subsequently contracted and fragmented by myosin, and the cortex ruptures, clears from most of the membrane area, and accumulates at multiple foci. Thus, we expect that a possible effect of Cyto-D is to decrease the entropy production rate. In Fig. 3 we show the effect of Cyto-D on the entropy production rate. We indeed find a decrease in activity. The decrease of the mean value of the measured activity is smaller than the decrease measured for ATP depletion.

Note that the probability distribution function of entropy generation rate has an exponential tail. We have found a significant number of patches with estimates of σ at least five times higher than the mean value (See Appendix A 3). As our measurements find set a lower bound to the actual entropy production rate, it is likely that in reality the PDF falls off even slower than an exponential. This underscores the heterogeneous nature of the activity of the membrane.

IV. DISCUSSION

Our attempt to tease out the essential nonequilibrium feature from flickering by using the entropy production rate as a measure of activity has a clear advantage over earlier methods, such as the ones dependent on the breakdown of the fluctuation-dissipation relation, e.g., Refs. [9,45–47]. First, the entropy production rate is the crucial measure of nonequilibrium—if a system A has a higher entropy production rate than a system B, then A is *further away* from equilibrium than B. Second, we are able to spatiotemporally resolve the entropy production rate, and are thereby able to identify regions that have a higher entropy production rate. This has not been achieved before. Third, our method gives a model-independent estimate of the lower bound of entropy production, whereas Refs. [9,48] must use a model for active fluctuations. Finally, the measurements in Refs. [9,45–48] are typically invasive in nature—they involve tracking the response of microscopic beads attached to systems and external perturbations [11] or attaching fluorescent proteins or filaments to the relevant degrees of freedom [12,13]. In contrast, our analysis is less invasive and is applicable to movies made by exploiting the naturally existing intracellular contrast [14,28].

Several comments are now in order. First, on the role of noise in our data: Clearly, if we apply our algorithm to patches outside the cell, we would obtain a small but nonzero number. We define a signal-to-noise ratio to be the activity obtained for patches inside the cell over patches outside the cell. We calculate this for patches of different sizes and find that the signal-to-noise ratio is maximum for patches of size $2\,\mu m^2$ [See Appendix A 1]. All the results we show in this paper uses

this size. Furthermore, for this patch size the activity grows linearly with the area of the membrane. See Appendix A 1.

Second, in addition to the necessary spatiotemporal coarse graining, which is part of any experimental measurement, we have performed a dimensional reduction by using principal component analysis and retained the first few components. How many principal components must we keep? We use a method proposed in Ref. [28]. We randomly shuffle our data along the time axis and then again calculate the eigenvalues of the correlation matrix. We find that the eigenvalues of this shuffled data are very close to one another. These set the noise floor of our measurements of principal components. Now, going back to the eigenvalues calculated from the original data, we find that only the first few—at most ten—eigenvalues are significantly larger than the noise floor (see Appendix A 2). Next, let us consider the algorithm where we assumed the optimal function to be a linear function of the currents. We limit our analysis to the first two principal components. Increasing the number of components to 10 does not have any significant effect on the estimated value of σ. For the second algorithm, where we used a neural network representation, the estimate of σ changes as the number of components is increased from two to ten, *during the training stage*, but yielded minimal change in the *testing stage*. Nonetheless, we retained the first ten components for all the results shown in this paper. The estimates of σ obtained by the two algorithms are comparable; the neural-network-based estimates are slightly higher. Furthermore, these also have better signal-to-noise ratio between the cell and the background.

Third, we compare our findings with the already known estimates of entropy production rates in microscopic biological systems. To the best of our knowledge there are no results for HeLA cells. Measurements that tracked a single filament of microtubules report an entropy production rate of $5\,k_B\,\mathrm{min}^{-1}$ [32] while a single actin fiber contracted by myosin motors reports an entropy production rate, per unit length, to be $\sim 1\ k_B/(\mu\mathrm{m}\,s)$ [49]. At the level of cells, e.g., in Ref. [33], the entropy production rate was quantified from experimental recordings of spontaneous hair-bundle oscillations in mechanosensory hair cells from the ear of the bullfrog. Interestingly, by applying (1), without any optimization over the current, the study found entropy productions of the order of $10^3\,k_B\,s^{-1}$. Another recent work [48] that analyzes flickering data from circumference of RBCs in a model-dependent fashion finds an entropy production rate of $\sim 10^6\,k_B\,s^{-1}$. This estimate depends on the details of the model used for cell flickering. However, it is argued to be compatible with microcalorimetric measurements of heat generation from packed RBCs in bulk [50,51]. In contrast, we find an average entropy production rate of $\sim 4\times 10^{-3}\,k_B\,s^{-1}$ over a 2-$\mu\mathrm{m}^2$ patch of the membrane. The distribution of the entropy production rate over patches features a fat tail to the right, and there are a significant number of patches with activities up to five times higher than the mean value (see Appendix A 3). Multiplying just the mean with the area of the basal membrane ($\sim 10^3\,\mu\mathrm{m}^2$), we find an estimate close to a few k_B per second. Although this is at least an order of magnitude higher than the numbers reported in Ref. [32], who used measurements of calcium flicker trajectories from single cells reported in Ref. [52], these values are several orders of magnitude lower than Refs. [33,48]. There may be several reasons for the low estimates we obtain, but the obvious reasons appear to be high noise levels in the experimental data and lower bounds of the estimate in Eq. (2) resulting from the necessary spatiotemporal coarse graining and dimensional reduction. Furthermore, we reiterate that the goal of our paper is not to calculate the total entropy production by all nonequilibrium processes in a cell—our focus is solely on the cell membrane. We do expect values significantly smaller than the total rate of consumption of ATPs in a cell because the membrane fluctuations are just one nonequilibrium process among many that goes on in a living cell.

Fourth, can we estimate the time scales of the active processes that play the most significant role in entropy generation? Unlike many of the cases listed above, the flickering data does not contain any clear "active spikes." This may be because multiple active processes with a range of time scales (0.1–2 s [9,37]) act on the membrane. Furthermore, an estimate of time scales is necessarily model dependent. We have analyzed such a model to obtain a closed-form estimate for the entropy production rate, and argue why it cannot be reliably applied to experimental data. See Appendix B for details.

In summary, there are a couple of areas that could benefit from further studies. Firstly, the entropy generation rate we obtained may be too small to be relevant for the metabolic processes of the whole cell. This could be attributed to the high noise level in our data; at most, only the first ten, sometimes even just the first two, principal components contain useful information. Thus, we anticipate that with improved resolution, our approach may unveil a significantly larger entropy generation rate. Secondly, the effect of Cyto-D on the entropy generation rate is quite small. Despite the significant impact of the acto-myosin cytoskeleton, which is notably affected by Cyto-D, the most active fluctuations of the membrane remain largely unchanged. Consequently, although we expected Cyto-D to substantially alter the entropy production rate, this is not the case. At present, we do not fully comprehend this aspect of our results.

To end on a positive note, besides capturing the cell-level activity, we report, for the first time, a spatiotemporally resolved activity. As shown in Fig. 2, cells have high activity regions which disappear on ATP depletion. This offers explicit evidence of heterogeneity of activity in the cell membrane, pointing to a lack of rapid establishment of a statistically homogeneous (although nonequilibrium) state. This technique can be combined with fluorescence imaging of a variety of "active" proteins or structures to measure their localized action. Thus, comparing maps of lateral organization of molecules of interest with activity maps could potentially identify those involved in actively regulating processes such as cell migration, endocytosis, and mechano-sensing.

ACKNOWLEDGMENTS

S.K.M. acknowledges the Knut and Alice Wallenberg Foundation for financial support through Grant No. KAW 2021.0328. In this study, part of the work was conducted by S.K.M. while at NORDITA, and the remaining part was carried out while the author was affiliated with Stanford

University. NORDITA is partially supported by Nordforsk. D.M. acknowledges the support of the Swedish Research Council Grants No. 638-2013-9243 and No. 2016-05225. B.S. acknowledges support from a Wellcome Trust/DBT India Alliance fellowship (Grant No. IA/I/13/1/500885) and CSRP from CEFIPRA (Grant No. 6303-1). T.G. thanks CEFIPRA for a scholarship. T.M. is supported by a predoctoral fellowship from the Council of Scientific and Industrial Research (CSIR), India.

APPENDIX A: INFERENCE ALGORITHMS

We first considered a particle swarm-based algorithm to perform the maximization

$$\sigma = 2k_{\mathrm{B}} \max_{J} \left[\frac{\langle J_{\Delta t} \rangle^2}{\Delta t \, \mathrm{Var}(J_{\Delta t})} \right]. \tag{A1}$$

Here, $J_{\Delta t}$ is calculated over time Δt, and the mean and the variance are calculated over an ensemble of such time intervals. Explicitly, we are searching over the phase space of the first few PCA components (see Appendix A 2), and currents constructed using a linear basis. We defined an N-dimensional vector $\boldsymbol{d}(\boldsymbol{\mathcal{I}})$ as a linear combination of the components of $\boldsymbol{\mathcal{I}}$, i.e.,

$$d_\alpha(\boldsymbol{\mathcal{I}}) = c_{\alpha\beta}\mathcal{I}_\beta, \tag{A2}$$

where the matrix $c_{\alpha\beta}$ consists of constant coefficients. At time $t = i\Delta t$, we define a scalar current:

$$J_{\Delta t}(t_i) \equiv \boldsymbol{d}\left(\frac{\boldsymbol{\mathcal{I}}(t_i + \Delta t) + \boldsymbol{\mathcal{I}}(t_i)}{2} \right) [\boldsymbol{\mathcal{I}}(t_i + \Delta t) - \boldsymbol{\mathcal{I}}(t_i)]. \tag{A3}$$

While using the particle swarm algorithm, we fixed $N = 2$. Increasing the number of components did not have a significant effect on the estimates of entropy production rate, primarily due to the presence of experimental noise. The details of the algorithm can be found in Ref. [38].

Linear representations of the function $\boldsymbol{d}(\boldsymbol{\mathcal{I}})$ such as the above severely limits the phase space of currents we are working with. Ideally, we should consider models which are more generic in the sense of having a nonlinear basis, and straightforwardly scalable to an arbitrary number of principal components. The most natural choice is to use a neural network. Hence, we have performed an independent estimation of the entropy production rate by using a neural network to represent the vector $\boldsymbol{d}(\boldsymbol{\mathcal{I}})$. The network architecture we used consists of two fully connected layers with a hyperbolic tangent (Tanh) activation function applied after each layer. The input dimension (`x_dim`) is set to N, and the number of nodes in the hidden layer (`nb_nodes`) is set to 256. For any input, this network returns an N-dimensional, nonlinear representation of the vector $\boldsymbol{d} := \boldsymbol{d}(\mathcal{I}|\boldsymbol{\theta})$, where $\boldsymbol{\theta}$ are the parameters of the neural network. The presence of the activation function tanh makes this representation arbitrarily nonlinear and bounded.

In Algorithm 1, we provide a schematic summary of the inference scheme with the neural network model. The hyperparameters of the algorithm, such as the number of nodes in the hidden layer, the number of principal components used, and the number of steps used for training are chosen by trying to maximize the signal-to-noise ratio between the estimate of entropy production rate between the cell and the background. Crucially, we have also used a data-splitting scheme where the first half of the data is used for training the model and the second half of the data is used to estimate entropy production rate using the trained model. See Ref. [31] for details. This approach helps overcome issues of overfitting to the data, which can lead to very high estimates of dissipation. Overfitting was also found to happen when the training was done for a large number of steps. Hence, we limited the number of steps in training to 100. With the data-splitting scheme, we get estimates of dissipation that are consistent with the estimates obtained using the particle swarm algorithm. See Fig. 4 for the comparison of results between the two algorithms. Results for more cells using both algorithms are shown in the Supplemental Material [41].

ALGORITHM 1. Train the model function $\boldsymbol{d}(\mathcal{I}|\boldsymbol{\theta})$.

Require: N-dimensional trajectories with length $N_f \Delta t$

$$\mathcal{I}^{(i)}(t) = \{\mathcal{I}_0^{(i)}, \mathcal{I}_{\Delta t}^{(i)}, ..., \mathcal{I}_{N_f \Delta t}^{(i)}\} (i = 1, ..., N)$$

Choose a hyperparameter set `nb_nodes`
$\boldsymbol{\theta} \leftarrow$ initialize network parameters
loop
Compute the current using $\boldsymbol{\mathcal{I}}(t)|_{t=0}^{N_f \Delta t/2}$

$$\{J_{\Delta t,j}\}_{j=1}^{N_f/2} = \left\{ \boldsymbol{d}\left(\tfrac{\boldsymbol{\mathcal{I}}_{j\Delta t} + \boldsymbol{\mathcal{I}}_{(j+1)\Delta t}}{2} | \boldsymbol{\theta} \right) \cdot (\boldsymbol{\mathcal{I}}_{(j+1)\Delta t} - \boldsymbol{\mathcal{I}}_{j\Delta t}) \right\}$$

Compute the objective function

$$\widehat{f}(\boldsymbol{\theta})|_{\mathrm{train}} = \left[\tfrac{2k_B \langle J_{\Delta t} \rangle^2}{\Delta t \, \mathrm{Var}(J_{\Delta t})} \right]$$

Update the parameters to maximize $\widehat{f}$
end loop
$\boldsymbol{\theta}^* \leftarrow$ parameters that maximize $\widehat{f}(\boldsymbol{\theta})|_{\mathrm{train}}$ in the record
Compute the test value $\widehat{f}(\boldsymbol{\theta}^*)|_{\mathrm{test}}$ using $\boldsymbol{\mathcal{I}}(t)|_{t=N_f \Delta t/2}^{N_f \Delta t}$.
return $\hat{\sigma} = \widehat{f}(\boldsymbol{\theta}^*)|_{\mathrm{test}}$

1. Dependence of the entropy estimate on the patch size

In Fig. 5, we summarize our analysis of how entropy production estimates depend on the cell area. We identified an optimal patch size of 20×20 pixels (approximately $2\,\mu\mathrm{m}^2$), which yielded the highest signal-to-noise ratio when comparing activity within the FBR region to background values. For this optimal patch size, we further found that entropy production computed over the entire cell membrane increases linearly with the membrane's area (number of patches).

2. Principal component analysis

Here, we demonstrate that the principal components other than the first few do not significantly contribute to the dynamics. We consider the data corresponding to the first cell in Fig. 2 of the main text. In Fig. 6, we plot the first 20 eigenvalues corresponding to PCA components for the normalized experimental data (blue) and the normalized data randomly shuffled along the time axis (purple). The error bars repre-

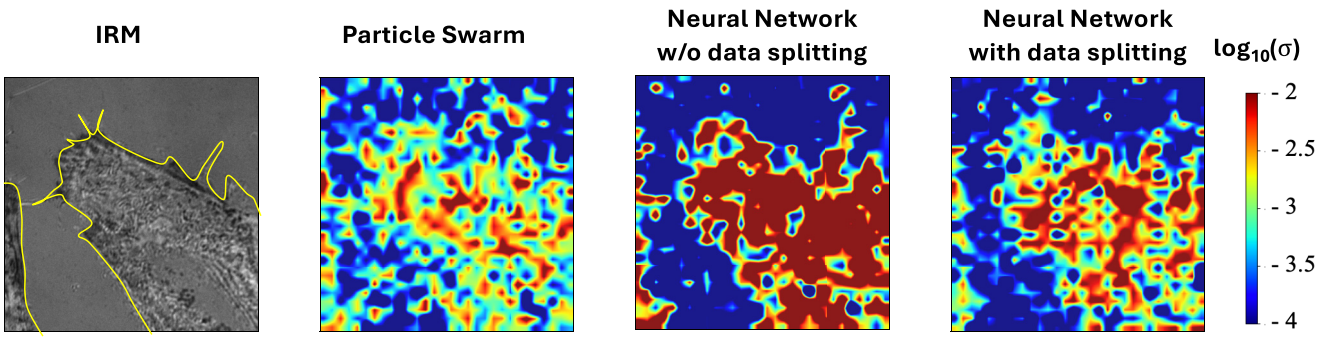

FIG. 4. The figure illustrates comparisons of entropy production rate estimates obtained using different algorithms: particle swarm algorithm, which takes in as input the first two principal components of IRM data, and neural-network-based algorithm, which takes as input the first ten principal components. While the neural-network-based algorithm, without a data-splitting scheme, produced the highest estimate, discerning overfitting effects is challenging. Conversely, estimates acquired using neural networks following the data-splitting scheme were lower but comparable in order of magnitude and slightly higher in values to those obtained from the particle swarm algorithm. Thus, we have presented results only from the neural network with data splitting and the particle swarm algorithm.

sent the standard deviation over different patches. The PCA eigenvalues for the shuffled data show the noise level in the system [28], which is slightly above zero. We observe that the eigenvalues rapidly decrease in magnitude and reach the noise levels within the first few principal components. This indicates that the principal components other than the first few closely approach the noise floor and do not significantly contribute to the dynamics.

3. Percentile averages

Due to significant inhomogeneity across the cell surface, relying solely on the mean value of the entropy production rate over patches may be inadequate. Hence, here we look at percentile averages, where we plot the average σ over the top $x\%$ of patches of the control cells. As shown in Fig. 7, the average of the top 10% of patches is nearly five times higher than the mean, and the average of the top 50% of patches is nearly double.

APPENDIX B: ENTROPY PRODUCTION RATE IN A MODEL OF ACTIVE MEMBRANE

We calculate the entropy production rate for an elementary model of active membrane [53]. Usually, flickering data is interpreted with a model [3,54,55] where the membrane is described by a height field $h(x, y)$ above the $x - y$ plane in Monge gauge described by the Hamiltonian

$$\mathcal{H}[h] = \int dxdy\Big[\frac{\gamma}{2}|\nabla h|^2 + \frac{\kappa}{2}(\nabla^2 h)^2\Big], \qquad \text{(B1)}$$

in equilibrium at temperature T. Here, γ is the surface tension and κ is the bending rigidity of the membrane. As the fluctuations of h are small, the model uses a small deformation approximation of curvature. We shall call this the Gaussian

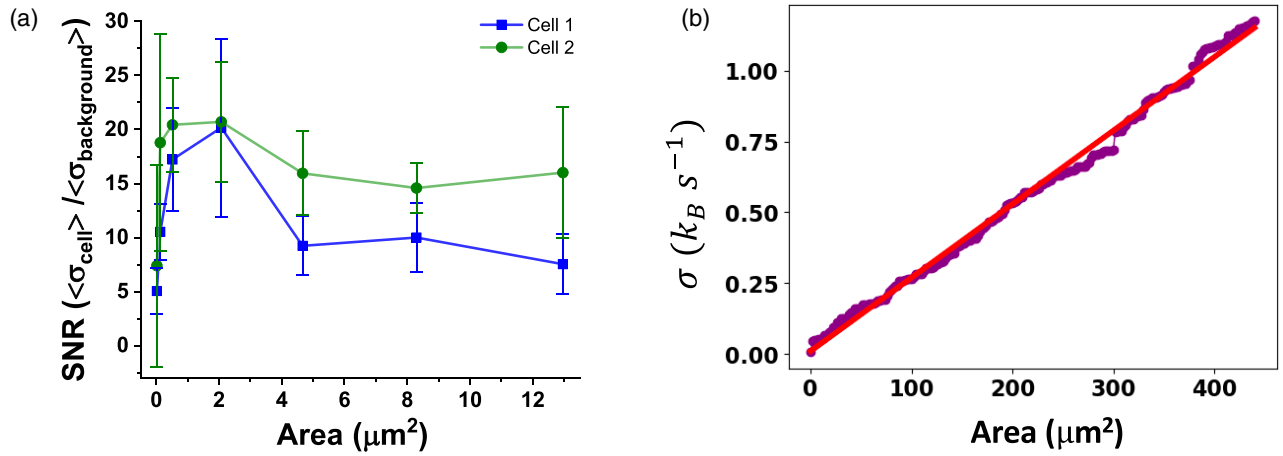

FIG. 5. (a) The signal-to-noise ratio computed by comparing the ratio of activity inferred in the FBR region with the corresponding value for the background. We find that the patch size 20×20 pixels or $\sim 2\ \mu m^2$ has the best signal-to-noise ratio. (b) The dependence of the entropy production rate on the area of the cell membrane for the optimal patch size (20×20 pixels). We observe that the estimate increases approximately linearly with the area.

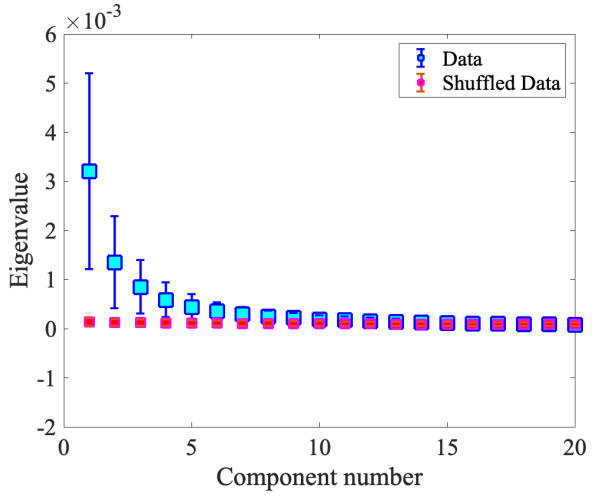

FIG. 6. Plots of the first 20 eigenvalues corresponding to PCA components, for the normalized experimental data (blue) and the normalized data randomly shuffled along the time axis (purple), for a representative cell flickering data. The error bars correspond to one standard deviation over different patches. The PCA eigenvalues for data shuffled along the time axis show the noise level in the system [28], which lies slightly above zero. We see that the magnitude of the eigenvalues rapidly drop and reach the noise levels within the first few principal components.

model. The Hamiltonian is diagonal in Fourier space. In the same spirit as Refs. [8,9,53], we write an active version of this model by writing an equation of motion for each Fourier mode $\hat{h}(\boldsymbol{q},t)$ coupled to an Ornstein-Uhlenbeck noise [56] $\lambda(\boldsymbol{q},t)$ as

$$\frac{\partial \hat{h}(\boldsymbol{q},t)}{\partial t} + \frac{1}{\tau(\boldsymbol{q})}\,\hat{h}(\boldsymbol{q},t) + b\,\lambda(\boldsymbol{q},t) = \sqrt{2D}\,\zeta(\boldsymbol{q},t) \quad \text{(B2a)}$$

$$\frac{\partial \lambda(\boldsymbol{q},t)}{\partial t} + \frac{1}{\tau_{\mathrm{A}}}\,\lambda(\boldsymbol{q}) = \sqrt{2D_{\mathrm{A}}}\,\zeta_{\mathrm{A}}(\boldsymbol{q},t), \quad \text{(B2b)}$$

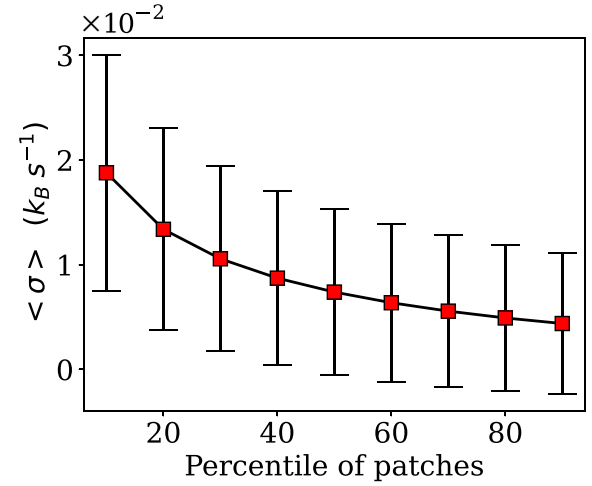

FIG. 7. The average σ over the top x% of patches of the control cells. Error bar corresponds to the standard deviation. We observe that the average of the top 10% of patches is nearly five times higher than the mean, and the average of the top 50% of patches is nearly double. Data is from one set of experiments using 14 cells. Two independent repeats show a similar trend.

where $\tau(\boldsymbol{q}) = \dfrac{4\eta q}{\kappa q^4 + \gamma q^2}$, (B2c)

$$\langle \zeta(\boldsymbol{q},t)\zeta(-\boldsymbol{q},s)\rangle = 2D(\boldsymbol{q})\delta(t-s), \quad \text{(B2d)}$$

$$\langle \zeta_{\mathrm{A}}(\boldsymbol{q},t)\zeta_{\mathrm{A}}(-\boldsymbol{q},s)\rangle = \delta(t-s), \text{ and} \quad \text{(B2e)}$$

$$D(\boldsymbol{q}) = \frac{k_{\mathrm{B}}T}{4\eta q}. \quad \text{(B2f)}$$

The membrane is assumed to undergo a stochastically driven overdamped motion. The viscosity of the fluid around the membrane is η, which is related to the amplitude of the stochastic driving ζ by fluctuation-dissipation theorem (B2f). In addition, there is active noise ζ_{A}, which is assumed to be white in space, and an Ornstein-Uhlenbeck noise (B2b) in time with a correlation time τ_{A} and an amplitude D_{A}. This active noise models both active processes on the membrane [53], e.g., opening of ion channels, endo and exo cytosis, etc., and driving by the cytoskelton [9]. In (B2a), we use the parameter b (of dimension s^{-1}) to determine the strength of the coupling of the membrane to the active fluctuations. Note that there are other models of time-correlated noises used to model active fluctuations in living systems. In Refs. [8,9,53], the active noise is modeled using a random telegraph process [57], which leads to the same exponential correlation in time for the noise as the Ornstein-Uhlenbeck process. In Refs. [58–60] the Ornstein-Uhlenbeck model itself is used.

For simplicity, from here onward, we drop the $\boldsymbol{q}$ dependence of ζ_{A}, τ_{A}, and D_{A}. As we have ignored nonlinearities in the model for the membrane, every $\hat{h}(\boldsymbol{q})$ is independent of every other $\hat{h}(\boldsymbol{q})$. Consequently, the total entropy production rate is a sum over all $\boldsymbol{q}$,

$$\sigma = \sum \sigma_{\boldsymbol{q}}. \quad \text{(B3)}$$

The individual terms in the sum corresponding to the entropy production rate for Eqs. (B2a) and (B2b) can be calculated analytically [61,62], by mapping to a well-studied model in stochastic thermodynamics [38,63,64]. We obtain

$$\sigma_{\boldsymbol{q}} = 2k_{\mathrm{B}}\,\frac{b^2 D_{\mathrm{A}}\tau(\boldsymbol{q})\tau_{\mathrm{A}}}{D(\tau(\boldsymbol{q})+\tau_{\mathrm{A}})} \quad \text{(B4a)}$$

$$= \frac{2k_{\mathrm{B}}}{\tau_{\mathrm{A}}(\boldsymbol{q})}\left[\frac{S(\boldsymbol{q})|_{\mathrm{A}}}{S(\boldsymbol{q})|_{\mathrm{Eq}}} - 1\right]. \quad \text{(B4b)}$$

In (B4b) the subscript "A" denotes the variance being calculated for an active membrane ($b \neq 0$), whereas the subscript "Eq" denotes the variance being calculated for a membrane in thermal equilibrium, i.e., $b = 0$. They can be computed from the knowledge of the stationary distribution of $\hat{h}$ and λ as [63,65]

$$S(\boldsymbol{q})|_{\mathrm{A}} = \langle \hat{h}^*(\boldsymbol{q})\hat{h}(\boldsymbol{q})\rangle = D\tau(\boldsymbol{q}) + \frac{b^2 D_{\mathrm{A}}\tau(\boldsymbol{q})^2\tau_{\mathrm{A}}^2}{\tau+\tau_{\mathrm{A}}}. \quad \text{(B5)}$$

We remark that the entropy production rate remains finite in the white noise limit of the Ornstein-Uhlenbeck process.

Notice that, though the model provides an exact analytical expression (B4a) and an accessible form (B4b) for the entropy production rate, applying it on the experimental data is rather challenging. This is because we do not have access to either the active time scale τ_{A} nor the equilibrium fluctuations of the membrane $S(\boldsymbol{q})|_{\mathrm{Eq}}$. Furthermore, in reality, the mechanical

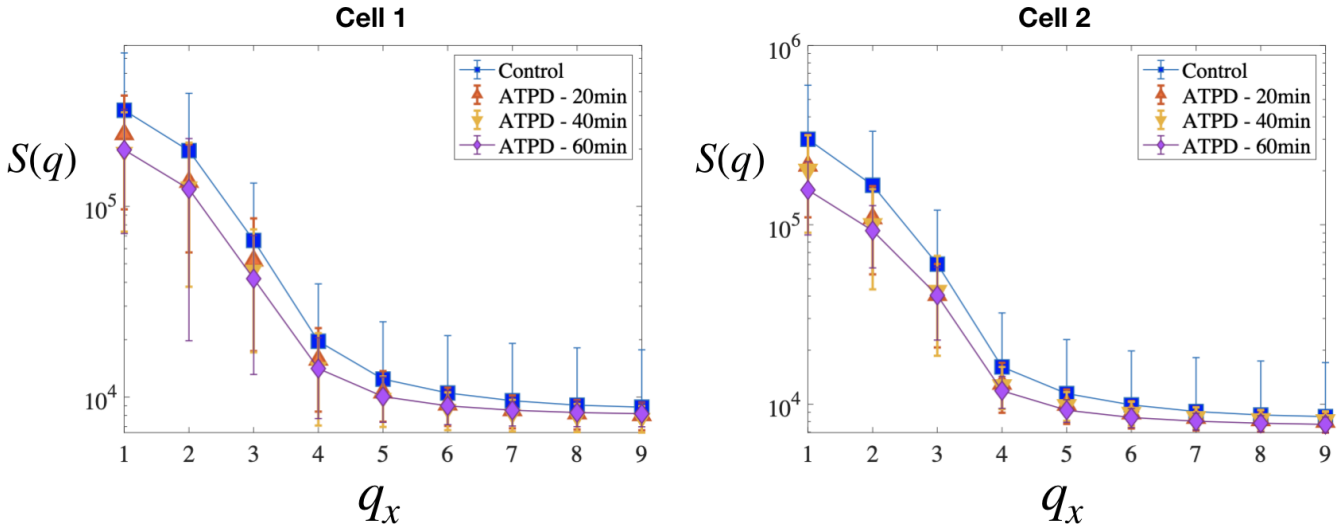

FIG. 8. The spectrum of height fluctuations $S(\boldsymbol{q})$ as a function of q in the horizontal direction for the two cells shown in Fig. 2 of the main paper. Different symbols denote different durations of ATP depletion.

properties of the membrane such as σ and κ could also change as a function of ATP depletion, and the model ignores any such possibility [66,67]. Nevertheless, assuming the model is representative of the actual membrane dynamics observed in the experiments, the following qualitative features can be deduced.

(1) The entropy production rate vanishes in the $D_A \to 0$ limit.

(2) The entropy production rate must be positive. Hence,

$$S(\boldsymbol{q})\big|_A \geqslant S(\boldsymbol{q})\big|_{Eq}. \tag{B6}$$

Assuming that the ATP depletion takes the cell membranes close to the equilibrium state, we can further argue that $S(\boldsymbol{q})|_A > S(\boldsymbol{q})|_{ATPD}$, where the subscript stands for the ATP-depleted cell membrane.

(3) The summation in (B3) should converge. Hence,

$$S(\boldsymbol{q})\big|_A \to S(\boldsymbol{q})\big|_{Eq} \text{ for large } q. \tag{B7}$$

As a corollary, we also obtain $S(\boldsymbol{q})|_A \to S(\boldsymbol{q})|_{ATPD}$ for large q.

Indeed, we find that fluctuations of the cell membranes we studied experimentally exhibit the qualitative features predicted by this model. We summarize our findings in Fig. 8 for the two cell samples in Fig. 2 of the main paper. For simplicity, we have only shown $S(\boldsymbol{q})|$ for $\boldsymbol{q}[0, i] \equiv q_x$ with $1 \leqslant i \leqslant 9$, and we find that it decreases as a function of ATP depletion in time for a fixed $\boldsymbol{q}$.

[1] E. Schrodinger, *What is Life? With Mind and Matter and Autobiographical Sketches* (Cambridge University Press, Cambridge, 2012).

[2] F. S. Gnesotto, F. Mura, J. Gladrow, and C. P. Broedersz, Broken detailed balance and non-equilibrium dynamics in living systems: A review, Rep. Prog. Phys. **81**, 066601 (2018).

[3] R. Phillips, J. Kondev, J. Theriot, H. G. Garcia, and N. Orme, *Physical Biology of the Cell* (Garland Science, New York, 2012).

[4] R. Blowers, E. M. Clarkson, and M. Maizels, Flicker phenomenon in human erythrocytes, J. Physiol. **113**, 228 (1951).

[5] S. Tuvia, A. Almagor, A. Bitler, S. Levin, R. Korenstein, and S. Yedgar, Cell membrane fluctuations are regulated by medium macroviscosity: Evidence for a metabolic driving force, Proc. Natl. Acad. Sci. USA **94**, 5045 (1997).

[6] T. Betz, M. Lenz, J.-F. Joanny, and C. Sykes, ATP-dependent mechanics of red blood cells, Proc. Natl. Acad. Sci. USA **106**, 15320 (2009).

[7] R. Rodríguez-García, I. López-Montero, M. Mell, G. Egea, N. S. Gov, and F. Monroy, Direct cytoskeleton forces cause membrane softening in red blood cells, Biophys. J. **108**, 2794 (2015).

[8] H. Turlier and T. Betz, Unveiling the active nature of living-membrane fluctuations and mechanics, Annu. Rev. Condens. Matter Phys. **10**, 213 (2019).

[9] H. Turlier, D. A. Fedosov, B. Audoly, T. Auth, N. S. Gov, C. Sykes, J.-F. Joanny, G. Gompper, and T. Betz, Equilibrium physics breakdown reveals the active nature of red blood cell flickering, Nat. Phys. **12**, 513 (2016).

[10] V. Ntziachristos, Going deeper than microscopy: The optical imaging frontier in biology, Nat. Methods **7**, 603 (2010).

[11] C. P. Brangwynne, G. H. Koenderink, F. C. MacKintosh, and D. A. Weitz, Cytoplasmic diffusion: Molecular motors mix it up, J. Cell Biol. **183**, 583 (2008).

[12] R. Yasuda, H. Noji, K. Kinosita Jr., and M. Yoshida, F_1-ATPase is a highly efficient molecular motor that rotates with discrete 120° steps, Cell **93**, 1117 (1998).

[13] R. Pepperkok and J. Ellenberg, High-throughput fluorescence microscopy for systems biology, Nat. Rev. Mol. Cell Biol. **7**, 690 (2006).

[14] Z. Wang, H. Ding, R. Bashir, G. Popescu, L. Millet, M. Gillette, and V. Chan, Label-free intracellular transport measured by spatial light interference microscopy, J Biomed. Opt. **16**, 026019 (2011).

[15] L. Basta, S. Veronesi, Y. Murata, Z. Dubois, N. Mishra, F. Fabbri, C. Coletti, and S. Heun, A sensitive calorimetric technique to study energy (heat) exchange at the nano-scale, Nanoscale **10**, 10079 (2018).

[16] C. Bustamante, J. Liphardt, and F. Ritort, The nonequilibrium thermodynamics of small systems, Phys. Today **58**(7), 43 (2005).

[17] C. Jarzynski, Equalities and inequalities: Irreversibility and the second law of thermodynamics at the nanoscale, Annu. Rev. Condens. Matter Phys. **2**, 329 (2011).

[18] U. Seifert, Stochastic thermodynamics, fluctuation theorems and molecular machines, Rep. Prog. Phys. **75**, 126001 (2012).

[19] J. M. Parrondo, C. Van den Broeck, and R. Kawai, Entropy production and the arrow of time, New J. Phys. **11**, 073008 (2009).

[20] M. Esposito, Stochastic thermodynamics under coarse graining, Phys. Rev. E **85**, 041125 (2012).

[21] M. Esposito, Erratum: Stochastic thermodynamics under coarse graining, Phys. Rev. E **86**, 049904 (2012).

[22] A. C. Barato and U. Seifert, Thermodynamic uncertainty relation for biomolecular processes, Phys. Rev. Lett. **114**, 158101 (2015).

[23] G. Bisker, M. Polettini, T. R. Gingrich, and J. M. Horowitz, Hierarchical bounds on entropy production inferred from partial information, J. Stat. Mech.: Theory Exp. (2017) 093210.

[24] I. Lestas, G. Vinnicombe, and J. Paulsson, Fundamental limits on the suppression of molecular fluctuations, Nature (London) **467**, 174 (2010).

[25] T. R. Gingrich, G. M. Rotskoff, and J. M. Horowitz, Inferring dissipation from current fluctuations, J. Phys. A: Math. Theor. **50**, 184004 (2017).

[26] J. M. Horowitz and T. R. Gingrich, Thermodynamic uncertainty relations constrain non-equilibrium fluctuations, Nat. Phys. **16**, 15 (2020).

[27] J. Li, J. M. Horowitz, T. R. Gingrich, and N. Fakhri, Quantifying dissipation using fluctuating currents, Nat. Commun. **10**, 1666 (2019).

[28] F. S. Gnesotto, G. Gradziuk, P. Ronceray, and C. P. Broedersz, Learning the non-equilibrium dynamics of Brownian movies, Nat. Commun. **11**, 5378 (2020).

[29] S. K. Manikandan, D. Gupta, and S. Krishnamurthy, Inferring entropy production from short experiments, Phys. Rev. Lett. **124**, 120603 (2020).

[30] A. Frishman and P. Ronceray, Learning force fields from stochastic trajectories, Phys. Rev. X **10**, 021009 (2020).

[31] S. Otsubo, S. K. Manikandan, T. Sagawa, and S. Krishnamurthy, Estimating time-dependent entropy production from non-equilibrium trajectories, Commun. Phys. **5**, 11 (2022).

[32] D. J. Skinner and J. Dunkel, Improved bounds on entropy production in living systems, Proc. Natl. Acad. Sci. USA **118**, e2024300118 (2021).

[33] É. Roldán, J. Barral, P. Martin, J. M. Parrondo, and F. Jülicher, Quantifying entropy production in active fluctuations of the hair-cell bundle from time irreversibility and uncertainty relations, New J. Phys. **23**, 083013 (2021).

[34] I. A. Martínez, G. Bisker, J. M. Horowitz, and J. M. Parrondo, Inferring broken detailed balance in the absence of observable currents, Nat. Commun. **10**, 1 (2019).

[35] S. Otsubo, S. Ito, A. Dechant, and T. Sagawa, Estimating entropy production by machine learning of short-time fluctuating currents, Phys. Rev. E **101**, 062106 (2020).

[36] T. Van Vu, V. Tuan Vo, and Y. Hasegawa, Entropy production estimation with optimal current, Phys. Rev. E **101**, 042138 (2020).

[37] A. Biswas, A. Alex, and B. Sinha, Mapping cell membrane fluctuations reveals their active regulation and transient heterogeneities, Biophys. J. **113**, 1768 (2017).

[38] S. K. Manikandan, S. Ghosh, A. Kundu, B. Das, V. Agrawal, D. Mitra, A. Banerjee, and S. Krishnamurthy, Quantitative analysis of non-equilibrium systems from short-time experimental data, Commun. Phys. **4**, 258 (2021).

[39] L. Limozin and K. Sengupta, Quantitative reflection interference contrast microscopy (RICM) in soft matter and cell adhesion, ChemPhysChem **10**, 2752 (2009).

[40] H.-F. Renard, M. Simunovic, J. Lemière, E. Boucrot, M. D. Garcia-Castillo, S. Arumugam, V. Chambon, C. Lamaze, C. Wunder, A. K. Kenworthy *et al.*, Endophilin-A2 functions in membrane scission in clathrin-independent endocytosis, Nature (London) **517**, 493 (2015).

[41] See Supplemental Material at http://link.aps.org/supplemental/10.1103/PhysRevResearch.6.023310 for several other representative examples and results obtained using two different algorithms.

[42] D. V. Köster and S. Mayor, Cortical actin and the plasma membrane: Inextricably intertwined, Curr. Opin. Cell Biol. **38**, 81 (2016).

[43] S. Dmitrieff and F. Nédélec, Amplification of actin polymerization forces, J. Cell Biol. **212**, 763 (2016).

[44] M. Schliwa, Action of cytochalasin D on cytoskeletal networks, J. Cell Biol. **92**, 79 (1982).

[45] T. Ariga, M. Tomishige, and D. Mizuno, Nonequilibrium energetics of molecular motor kinesin, Phys. Rev. Lett. **121**, 218101 (2018).

[46] T. Ariga, M. Tomishige, and D. Mizuno, Experimental and theoretical energetics of walking molecular motors under fluctuating environments, Biophys. Rev. **12**, 503 (2020).

[47] T. Ariga, K. Tateishi, M. Tomishige, and D. Mizuno, Noise-induced acceleration of single molecule kinesin-1, Phys. Rev. Lett. **127**, 178101 (2021).

[48] I. Di Terlizzi, M. Gironella, D. Herráez-Aguilar, T. Betz, F. Monroy, M. Baiesi, and F. Ritort, Variance sum rule for entropy production, Science **383**, 971 (2024).

[49] D. S. Seara, V. Yadav, I. Linsmeier, A. P. Tabatabai, P. W. Oakes, S. Tabei, S. Banerjee, and M. P. Murrell, Entropy production rate is maximized in non-contractile actomyosin, Nat. Commun. **9**, 4948 (2018).

[50] U. Bandmann, M. Monti, and I. Wadsö, Clinical physiology: Microcalorimetric measurements of heat production in whole blood and blood cells of normal persons, Scand. J. Clin. Lab. Invest. **35**, 121 (1975).

[51] P. Bäckman, A microcalorimetric study of human erythrocytes in stirred buffer suspensions, Thermochim. Acta **205**, 87 (1992).

[52] K. Thurley, S. C. Tovey, G. Moenke, V. L. Prince, A. Meena, A. P. Thomas, A. Skupin, C. W. Taylor, and M. Falcke, Reliable encoding of stimulus intensities within random sequences of intracellular Ca^{2+} spikes, Sci. Signal. **7**, ra59 (2014).

[53] J. Prost and R. Bruinsma, Shape fluctuations of active membranes, Europhys. Lett. **33**, 321 (1996).
[54] M. Müller, K. Katsov, and M. Schick, Biological and synthetic membranes: What can be learned from a coarse-grained description? Phys. Rep. **434**, 113 (2006).
[55] S. Safran, *Statistical Thermodynamics of Surfaces, Interfaces, and Membranes* (CRC Press, Boca Raton, 2018).
[56] S. Chandrasekhar, Stochastic problems in physics and astronomy, Rev. Mod. Phys. **15**, 1 (1943).
[57] C. W. Gardiner, *Handbook of Stochastic Methods* (Springer Berlin, 1985), Vol. 3.
[58] L. Dabelow, S. Bo, and R. Eichhorn, Irreversibility in active matter systems: Fluctuation theorem and mutual information, Phys. Rev. X **9**, 021009 (2019).
[59] L. Dabelow and R. Eichhorn, Irreversibility in active matter: General framework for active Ornstein-Uhlenbeck particles, Front. Phys. **8**, 516 (2021).
[60] L. Dabelow, S. Bo, and R. Eichhorn, How irreversible are steady-state trajectories of a trapped active particle? J. Stat. Mech.: Theory Exp. (2021) 033216.
[61] U. Seifert, Entropy production along a stochastic trajectory and an integral fluctuation theorem, Phys. Rev. Lett. **95**, 040602 (2005).
[62] S. Borlenghi, S. Iubini, S. Lepri, and J. Fransson, Entropy production for complex Langevin equations, Phys. Rev. E **96**, 012150 (2017).
[63] A. Pal and S. Sabhapandit, Work fluctuations for a Brownian particle in a harmonic trap with fluctuating locations, Phys. Rev. E **87**, 022138 (2013).
[64] S. K. Manikandan and S. Krishnamurthy, Exact results for the finite time thermodynamic uncertainty relation, J. Phys. A: Math. Theor. **51**, 11LT01 (2018).
[65] A. Argun, J. Soni, L. Dabelow, S. Bo, G. Pesce, R. Eichhorn, and G. Volpe, Experimental realization of a minimal microscopic heat engine, Phys. Rev. E **96**, 052106 (2017).
[66] R. J. Hawkins and T. B. Liverpool, Stress reorganization and response in active solids, Phys. Rev. Lett. **113**, 028102 (2014).
[67] B. Loubet, U. Seifert, and M. A. Lomholt, Effective tension and fluctuations in active membranes, Phys. Rev. E **85**, 031913 (2012).